SFN355#25–30

25	**Understanding star formation in molecular clouds IV. Column density PDFs from quiescent to massive molecular clouds** Schneider et al. (2022), A&A, 666 A165
26	**The First Detection of a Protostellar CO Outflow in the Small Magellanic Cloud with ALMA** Tokuda et al. (2022), ApJL, 936, L6
27	**Grain Growth During Protostellar Disk Formation** Tu, Li, Lam (2022), MNRAS, 515, 4780
28	**Distributed YSOs in the Perseus Molecular Cloud from the Gaia and LAMOST Surveys** Wang et al. (2022), ApJ, 936, 23
29	**Probing Magnetic Fields in Protoplanetary Disk Atmospheres through Polarized Optical/IR Light Scattered by Aligned Grains** Yang & Li (2022), AJ, 164, 99
30	**Characterising the orbit and circumstellar environment of the high-mass binary MWC 166 A** Zarrilli et al. (2022), A&A, 665, A146

SFN355#25

Understanding star formation in molecular clouds

IV. Column density PDFs from quiescent to massive molecular clouds

N. Schneider[1], V. Ossenkopf-Okada[1], S. Clarke[1,2], R. S. Klessen[3], S. Kabanovic[1], T. Veltchev[4], S. Bontemps[5], S. Dib[5,6], T. Csengeri[5], C. Federrath[7], J. Di Francesco[8,9], F. Motte[10], Ph. André[11], D. Arzoumanian[12], J. R. Beattie[7], L. Bonne[5,13], P. Didelon[11], D. Elia[14], V. Könyves[15], A. Kritsuk[16], B. Ladjelate[17], Ph. Myers[18], S. Pezzuto[14], J. F. Robitaille[10], A. Roy[5], D. Seifried[1], R. Simon[1], J. Soler[6], and D. Ward-Thompson[15]

ABSTRACT

Probability distribution functions of the total hydrogen column density (N-PDFs) are a valuable tool for distinguishing between the various processes (turbulence, gravity, radiative feedback, magnetic fields) governing the morphological and dynamical structure of the interstellar medium. We present N-PDFs of 29 Galactic regions obtained from *Herschel* imaging at high angular resolution (18″), covering diffuse and quiescent clouds, and those showing low-, intermediate-, and high-mass star formation (SF), and characterize the cloud structure using the Δ-variance tool. The N-PDFs show a large variety of morphologies. They are all double-log-normal at low column densities, and display one or two power law tails (PLTs) at higher column densities. For diffuse, quiescent, and low-mass SF clouds, we propose that the two log-normals arise from the atomic and molecular phase, respectively. For massive clouds, we suggest that the first log-normal is built up by turbulently mixed H_2 and the second one by compressed (via stellar feedback) molecular gas. Nearly all clouds have two PLTs with slopes consistent with self-gravity, where the second one can be flatter or steeper than the first one. A flatter PLT could be caused by stellar feedback or other physical processes that slow down collapse and reduce the flow of mass toward higher densities. The steeper slope could arise if the magnetic field is oriented perpendicular to the LOS column density distribution. The first deviation point (DP), where the N-PDF turns from log-normal into a PLT, shows a clustering around values of a visual extinction of A_V (DP1) ~ 2–5. The second DP, which defines the break between the two PLTs, varies strongly. In contrast, the width of the N-PDFs is the most stable parameter, with values of σ between ~0.5 and 0.6. Using the Δ-variance tool, we observe that the A_V value, where the slope changes between the first and second PLT, increases with the characteristic size scale in the Δ-variance spectrum. We conclude that at low column densities, atomic and molecular gas is turbulently mixed, while at high column densities, the gas is fully molecular and dominated by self-gravity. The best fitting model N-PDFs of molecular clouds is thus one with log-normal low column density distributions, followed by one or two PLTs.

N-PDF (水素原子柱密度の確率密度関数)

分子雲における星形成を特徴づける

- Log-normal … 等温超音速乱流が支えるガス雲
- Power law tail (PLT) … 自己重力による収縮

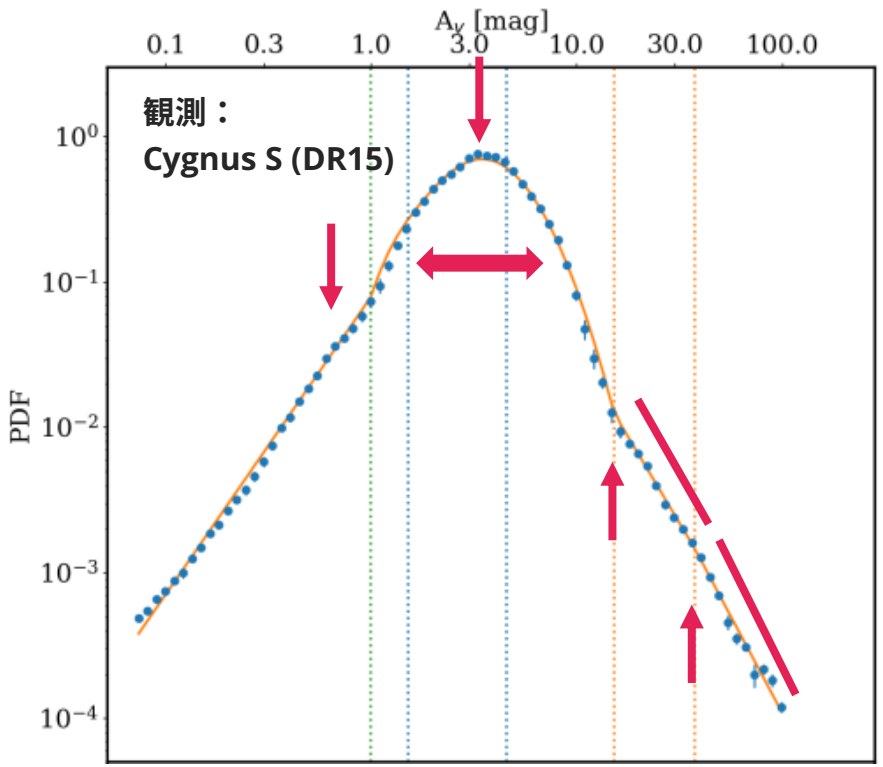

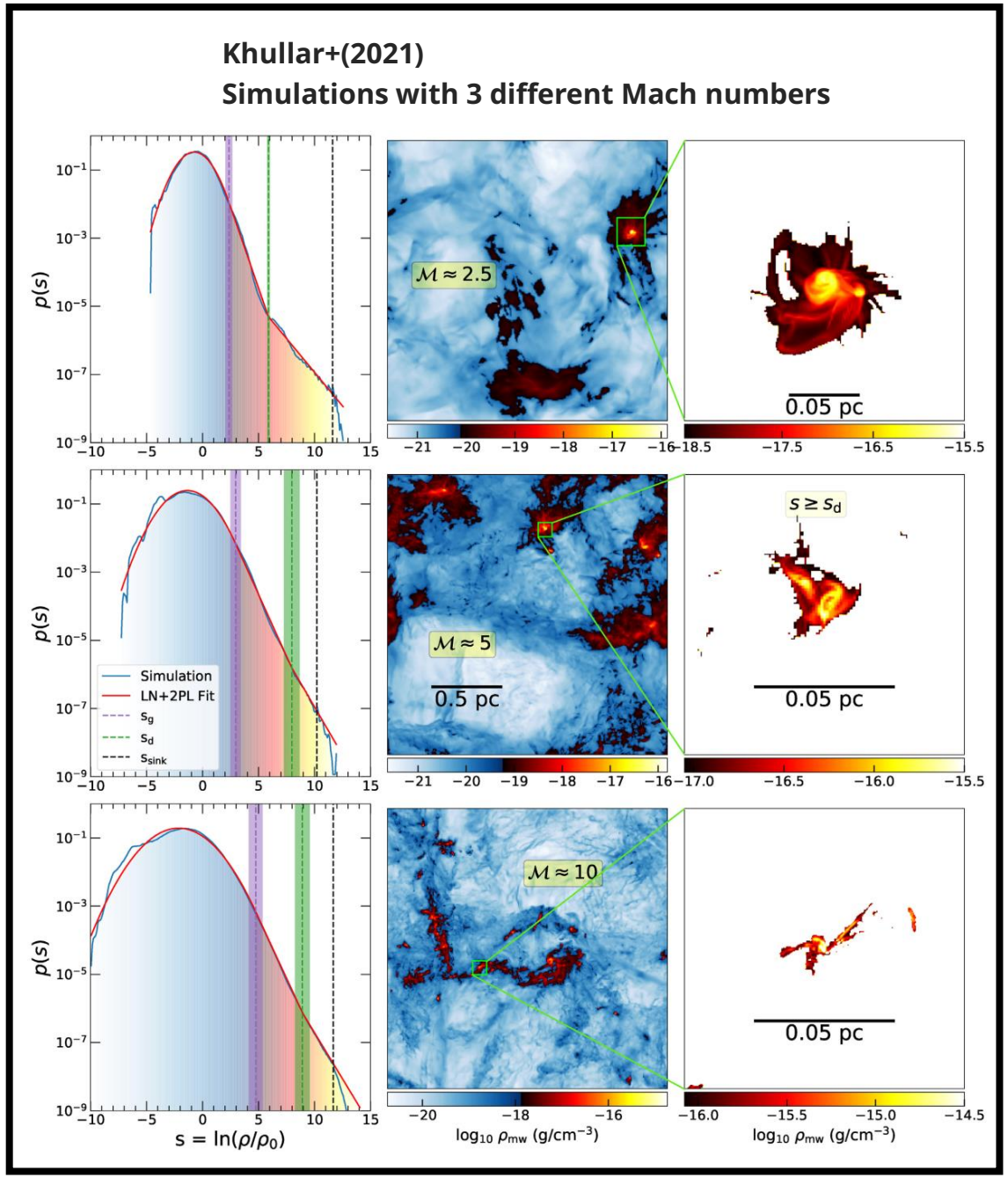

統計的アプローチ：Diffuse領域 ~ 大質量星形成領域

Paper I (Schneider+2015a) … N-PDFsへのline-of-sight contaminationの影響
Paper II (Schneider+2015b) … massive IRDCsのN-PDFs
Paper III (Schneider+2016) … 分子雲輝線観測から構築したN-PDFsの問題点
Paper IV (this paper) … 29の分子雲より得られた様々なN-PDFs

大質量星形成領域 (9)

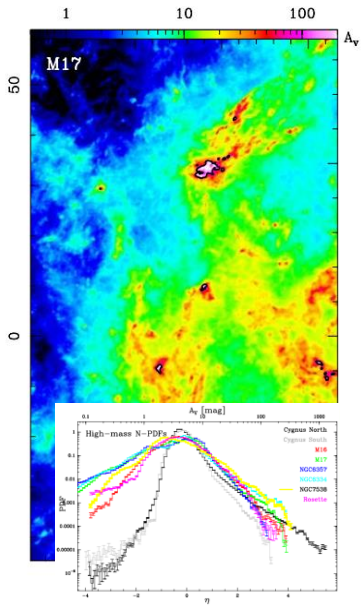

中間質量星形成領域 (6)

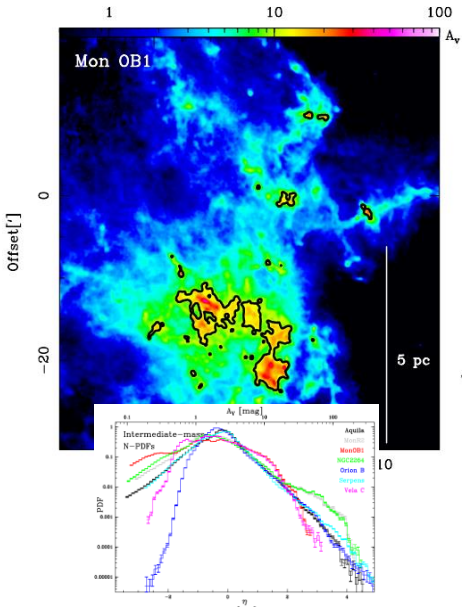

小質量星形成領域 (10)

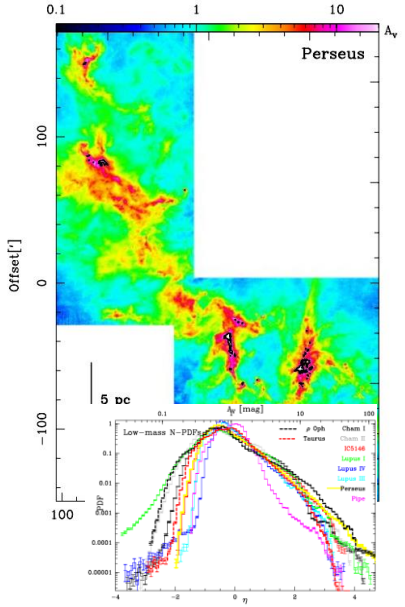

Quiescent領域 (3)

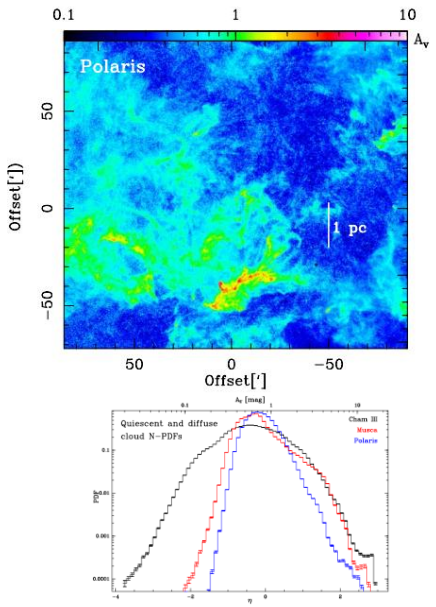

Diffuse/atomic領域 (1)

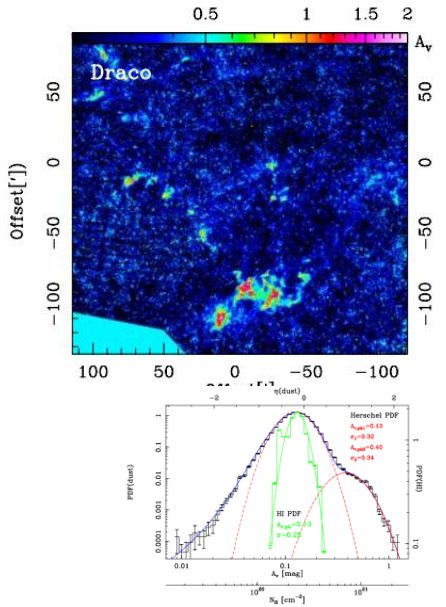

観測・データ解析

Herschelによる柱密度分布観測

- Herschel Gould Belt survey (HGBS; Andre+2010)
- Herschel imaging survey of OB Young Stellar objects (HOBYS; Motte+2010)
- Herschel Infrared GALactic plane survey (Hi-GAL; Molinari+2010)
- Individual PI programs

29の分子雲を選択。以下のように分類。

- 大質量　　… 巨大分子雲 (10^5-10^6 [M_{sun}], ~100 [pc])
- 中間質量　… 中間の分子雲 (10^4-10^5 [M_{sun}])
- 低質量　　… 分子雲 (10^3-10^4 [M_{sun}], ~数10 [pc])
- Quiescent　… 星形成活動が僅か
- Diffuse　　… ほぼ水素原子

Cloud	LOS Dust (mag) (1)	$\langle N(H_2)\rangle$ (10^{21} cm^{-2}) (2)	A $A_V > 1$ (pc^2) (3)	R (pc) (4)	$\langle n\rangle$ $A_V > 1$ (cm^{-3}) (5)	M $A_V > 1$ (10^3 $M_\odot$) (6)
High-mass SF regions						
Cygnus North	5.0	5.06	3417	33.0	24.9	324.46
Cygnus South	5.0	5.47	3731	34.5	25.7	383.45
M16	7.8	4.18	1057	18.3	36.9	87.12
M17	6.6	9.99	2478	28.1	57.7	483.76
NGC 6334	8.7	13.98	882	16.8	135.1	238.60
NGC 6357	4.2	7.22	1004	17.9	65.4	145.14
NGC 7538	3.3	4.22	1524	22.0	31.0	130.39
Rosette	1.1	4.10	881	16.8	39.7	70.64
Vela C	2.0	6.85	450	12.0	92.7	58.00
Intermediate-mass SF regions						
Aquila	2.5	2.74	445	11.9	37.3	25.94
Mon R2	1.6	2.00	82	5.1	63.3	4.60
Mon OB1	2.2	2.31	59	4.4	86.1	4.87
NGC 2264	1.6	2.60	169	7.3	57.5	11.12
Orion B	0.9	2.06	683	14.8	22.7	29.69
Serpens	1.6	1.46	266	10.8	21.9	14.15
Low-mass SF regions						
Cham I	0.25	1.07	18	2.4	72.5	0.767
Cham II	0.23	1.00	12	2.0	82.2	0.507
IC5146	0.37	1.07	121	6.2	28.0	5.03
Lupus I	0.17	0.82	6.6	1.4	91.7	0.364
Lupus III	0.44	1.16	5.0	1.3	148.9	0.180
Lupus VI	0.46	1.00	7.3	1.5	106.0	0.398
Perseus	0.66	1.62	174	7.4	35.3	4.350
Pipe	0.59	1.72	40	3.6	77.8	1.452
ρOph	1.25	1.57	26	2.9	89.0	1.244
Taurus	0.4	1.73	97	5.5	50.7	4.03
Quiescent regions						
Cham III	0.16	0.81	9.4	1.7	75.4	0.317
Musca	0.37	0.75	3.2	1.0	121.2	0.110
Polaris	0.31	1.73	11.3	1.9	31.9	1.208
Diffuse/atomic regions						
Draco[(a)]		0.60	1500	21.9	4.4	8.04

N-PDFsの関数fit

N-PDF毎に8つの関数モデルのbest fit parametersをMCMCより決定

- ELP, ELLP, EL2P, ELL2P, LP, LLP, L2P, LL2P

E (error slopes at low column densities), L (log-normals), LL (pairs of log-normals), P (power-law), 2P (double power laws)

例：Cygnus S (DR1
→ ELL2P

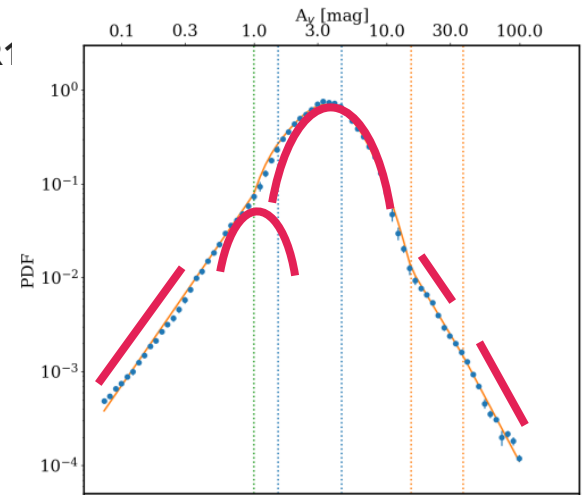

8モデル中のbest fir modelをベイズ情報量規準を用いて決定 (最小となるモデル)

$$\mathrm{BIC}(k) = k\ln(n) - 2\ln(\mathcal{L})$$

n ... N-PDFのデータ数
k ... モデルパラメータ数
L ... MCMCより求めた最大尤度

Cloud	Model (1)	$A_{V,pk1}$ (mag) (2)	$A_{V,pk2}$ (mag) (3)
High-mass SF regions			
Cygnus N	ELL2P	2.63	2.76
Cygnus S	ELL2P	1.39	3.46
M16	ELLP	3.17	3.55
M17	ELL2P	4.63	12.85
NGC 6334	ELL2P	4.90	14.95
NGC 6357	ELL2P	2.77	9.88
NGC 7538	ELL2P	1.75	3.13
Rosette	ELL2P	3.03	9.09
Vela C	ELL2P	4.64	3.80
mean		3.2 ± 1.2	7.1 ± 4.4
median		3.0	3.8
Intermediate-mass SF regions			
Aquila	ELL2P	1.42	2.77
Mon R2	ELL2P	0.84	1.71
Mon OB1	ELL2P	0.21	1.75
NGC 2264	ELL2P	1.64	1.62
Orion B	ELL2P	1.53	1.66
Serpens	ELL2P	0.66	1.43
mean		1.1 ± 0.5	1.8 ± 0.4
median		1.1	1.68
Low-mass SF regions			
Cham I	EL2P	0.47	–
Cham II	ELL2P	0.54	0.72
IC5146	ELL2P	0.71	0.82
Lupus I	ELL2P	0.44	0.63
Lupus III	ELL2P	0.91	0.93
Lupus IV	ELL2P	0.72	1.12
Perseus	L2P	1.04	–
Pipe	ELL2P	0.99	1.92
ρOph	LL2P	0.32	1.04
Taurus	LL2P	0.64	1.51
mean		0.7 ± 0.2	1.1 ± 0.4
median		0.7	0.99
Quiescent regions			
Cham III	ELL2P	0.53	0.64
Musca	LL2P	0.45	0.70
Polaris	ELL2P	0.45	0.62
mean		0.48 ± 0.04	0.65 ± 0.03
median		0.45	0.64
Diffuse/atomic regions			
Draco	LL	0.13	0.40

...

N-PDFs of all clouds

とても複雑。シミュレーションから得られる綺麗な形にはならない。
(定量的な解析を行うには十分な統計数ではない)

最も多い形は “2 log-normals + 2 power-law tails (PLTs)”

- 低密度側での2つのlog-normals : 分子雲における2成分
- 高密度側での2つのPLTs : 重力収縮への影響, 冪がflatter or steeperで異なる

大質量星形成領域 (9)

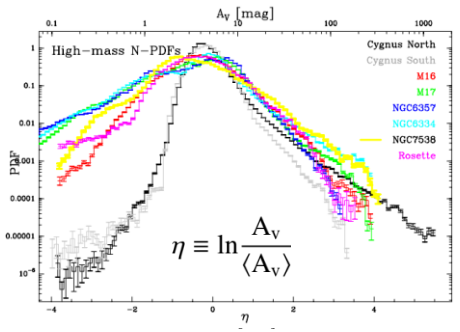

中間質量星形成領域 (6)

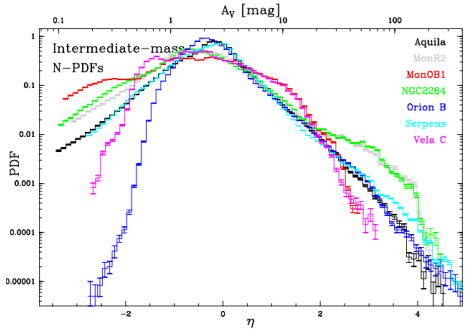

小質量星形成領域 (10)

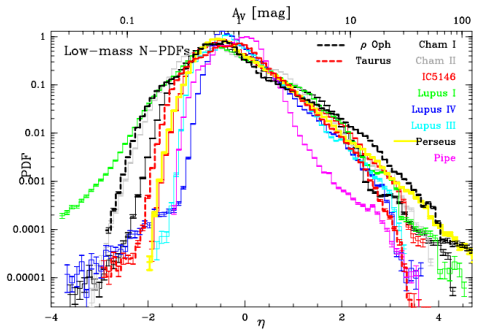

Quiescent領域 (3)

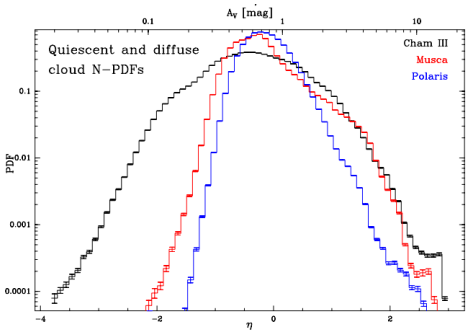

Diffuse/atomic領域 (1)

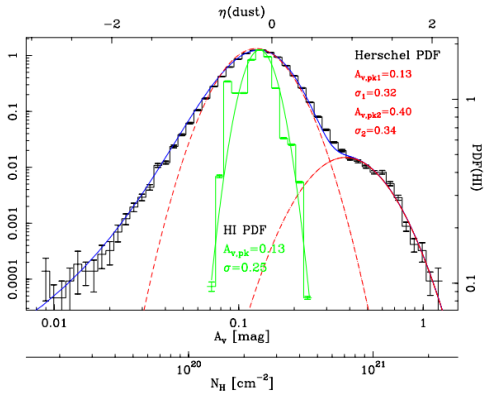

2 log-normals

大質量・中間質量星形成領域
(低密度側) H_2 gas
(高密度側) stellar feedback (HII region等) による圧縮

小質量星形成・Quiescent・Diffuse領域
(低密度側) HI gas
(高密度側) H_2 gas

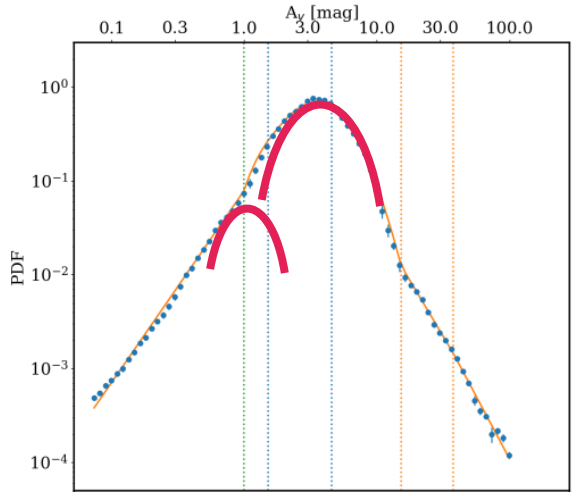

2 Power law tails (PLTs)

大質量・中間質量星形成領域
(PLT1) 重力収縮, s_1~2
(PLT2) 重力収縮, s_2~2

$$\rho \propto r^{-\alpha} \qquad \alpha = (-2/s) + 1$$

等温球密度分布の重力収縮 (α=2 ⇔ s=2)

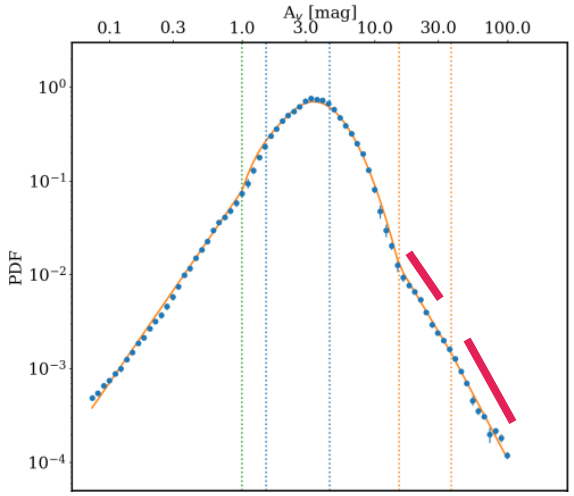

小質量星形成領域
(PLT1) 重力収縮
(PLT2) 8/10でsteeper, 柱密度分布と直交する磁場の影響?

磁場分布の観測はある
しかし数値シミュレーションでは確認されていない

Quiescent領域
- 3サンプル間で個性豊か

Diffuse領域
- なし

まとめ

	LN 1	LN2	PLT1	PLT2
Diffuse	HI gas	H_2 gas	×	×
Quiescent			3サンプルで様々	
Low-mass			重力収縮 (s~-2)	磁場? (s~-2.76)
Intermediate-mass	H_2 gas	Stellar feedback (HII region)による圧縮	重力収縮 (s~-2)	
High-mass				

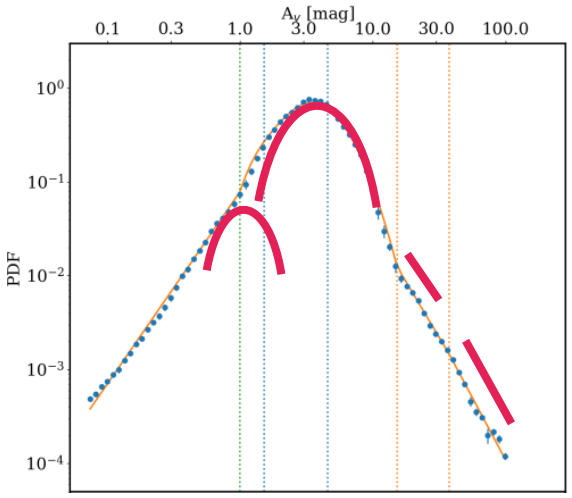

SFN355#26

The First Detection of a Protostellar CO Outflow in the Small Magellanic Cloud with ALMA

Kazuki Tokuda[1,2,3], Sarolta Zahorecz[2,3], Yuri Kunitoshi[3], Kosuke Higashino[3], Kei E. I. Tanaka[2,4], Ayu Konishi[3], Taisei Suzuki[3], Naoya Kitano[3], Naoto Harada[1], Takashi Shimonishi[5], Naslim Neelamkodan[6], Yasuo Fukui[7], Akiko Kawamura[2], Toshikazu Onishi[3], and Masahiro N. Machida[1]

Abstract

Protostellar outflows are one of the most outstanding features of star formation. Observational studies over the last several decades have successfully demonstrated that outflows are ubiquitously associated with low- and high-mass protostars in solar-metallicity Galactic conditions. However, the environmental dependence of protostellar outflow properties is still poorly understood, particularly in the low-metallicity regime. Here we report the first detection of a molecular outflow in the Small Magellanic Cloud with $0.2\,Z_{\odot}$, using Atacama Large Millimeter/submillimeter Array observations at a spatial resolution of 0.1 pc toward the massive protostar Y246. The bipolar outflow is nicely illustrated by high-velocity wings of CO(3–2) emission at $\gtrsim$15 km s^{-1}. The evaluated properties of the outflow (momentum, mechanical force, etc.) are consistent with those of the Galactic counterparts. Our results suggest that the molecular outflows, i.e., the guidepost of the disk accretion at the small scale, might be universally associated with protostars across the metallicity range of $\sim$0.2–1 $Z_{\odot}$.

九州大学 KYUSHU UNIVERSITY　大阪公立大学 Osaka Metropolitan University

PRESS RELEASE（2022/08/18）

19 万光年彼方の小マゼラン雲から星の産声をキャッチ！

アルマ望遠鏡が捉える 100 億年前相当の星の誕生

ポイント

① 太陽系誕生よりも遥か昔の環境でどのように恒星(星)が誕生するかが未解明であった
② 100 億年前相当の状況に近い小マゼラン雲で星誕生の産声を初めて検出することに成功
③ 産声を手がかりに、宇宙の遥か昔の星や惑星の誕生過程の解明がさらに進むと期待

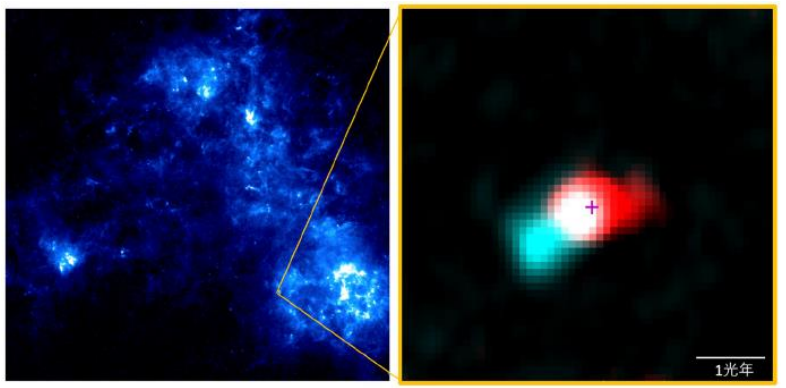

図 1: (左) 欧州宇宙機関のハーシェル宇宙天文台が遠赤外線で観測した小マゼラン雲と(右) 原始星 Y246 からの双極分子流。シアンおよび赤色で示した部分がそれぞれ地球に近づく方向および遠ざかる方向に時速 54000 km 以上の速さで運動しています。クロスは原始星の位置を示しています。
Credit: ALMA (ESO/NAOJ/NRAO), Tokuda et al. ESA/Herschel

SFN355#27

Grain growth during protostellar disc formation

Yisheng Tu ,★ Zhi-Yun Li and Ka Ho Lam

ABSTRACT

Recent observations indicate that mm/cm-sized grains may exist in the embedded protostellar discs. How such large grains grow from the micron size (or less) in the earliest phase of star formation remains relatively unexplored. In this study, we take a first step to model the grain growth in the protostellar environment, using 2D (axisymmetric) radiation hydrodynamic and grain growth simulations. We show that the grain growth calculations can be greatly simplified by the 'terminal velocity approximation', where the dust drift velocity relative to the gas is proportional to its stopping time, which is proportional to the grain size. We find that the grain–grain collision from size-dependent terminal velocity alone is too slow to convert a significant fraction of the initially micron-sized grains into mm/cm sizes during the deeply embedded Class 0 phase. Substantial grain growth is achieved when the grain–grain collision speed is enhanced by a factor of 4. The dust growth above and below the disc midplane enables the grains to settle faster towards the midplane, which increases the local dust-to-gas ratio, which, in turn, speeds up further growth there. How this needed enhancement can be achieved is unclear, although turbulence is a strong possibility that deserves further exploration.

星形成初期段階において、micron size (以下) のgrainがどこまで大きく成長できるか？

2D軸対称RHD + (post-process) grain growthシミュレーションを行った。

- ”terminal velocity approximation” (gasに対するdustのdrift velocityは(grain sizeに比例する)stopping timeに比例する) によって計算を簡略化

SFN355#28

Distributed YSOs in the Perseus Molecular Cloud from the Gaia and LAMOST Surveys

Xiao-Long Wang[1,2], Min Fang[1,3], Yu Gao[1,4,8], Hong-Xin Zhang[3,5], Gregory J. Herczeg[6,7], Hong-Jun Ma[1], En Chen[1,3], and Xing-Yu Zhou[6,7]

Abstract

Identifying the young optically visible population in a star-forming region is essential for fully understanding the star formation event. In this paper, we identify 211 candidate members of the Perseus molecular cloud based on Gaia astrometry. We use LAMOST spectra to confirm that 51 of these candidates are new members, bringing the total census of known members to 856. The newly confirmed members are less extincted than previously known members. Two new stellar aggregates are identified in our updated census. With the updated member list, we obtain a statistically significant distance gradient of 4.84 pc deg^{-1} from west to east. Distances and extinction corrected color–magnitude diagrams indicate that NGC 1333 is significantly younger than IC 348 and the remaining cloud regions. The disk fraction in NGC 1333 is higher than elsewhere, consistent with its youngest age. The star formation scenario in the Perseus molecular cloud is investigated and the bulk motion of the distributed population is consistent with the cloud being swept away by the Per-Tau Shell.

Perseus分子雲: ~300 [pc] from the Sun, 低質量星形成領域

Gaia EDR3 (位置天文学・測光データ)　... 新たなYSOs候補の特定
LAMOST DR7 (分光データ)　... 分子雲のメンバーであることを確認

Perseus分子雲のYSOs：Gaia

既知メンバー (805天体) の統計的性質を用いて、Gaiaカタログから候補天体を絞り込む。
➔ 211 candidate members

(a) 視差 (3σ以内)

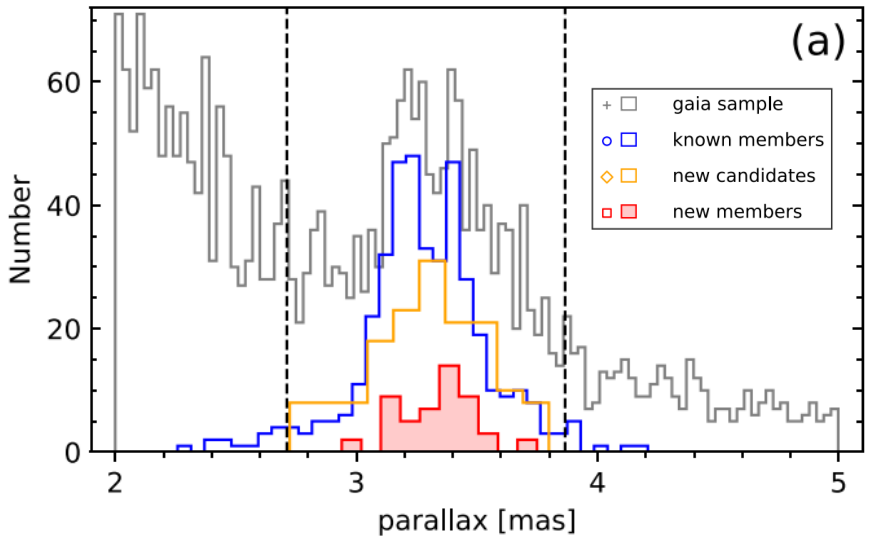

(b) 固有運動 (3σ以内)

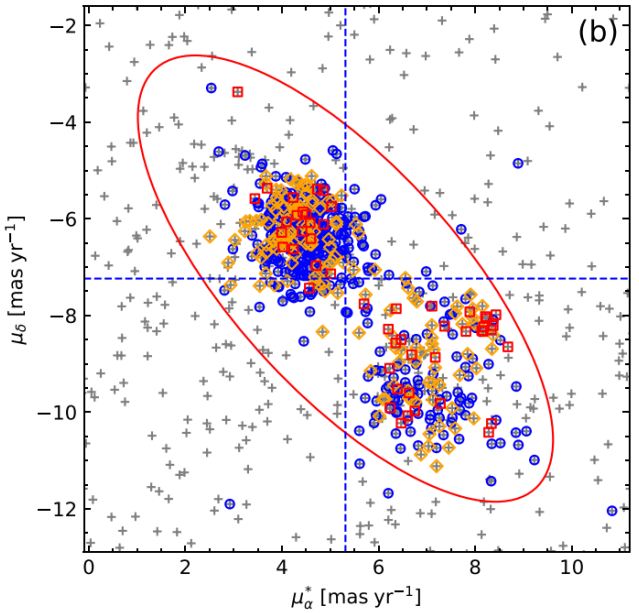

(c) 年齢 (10Myr以上)

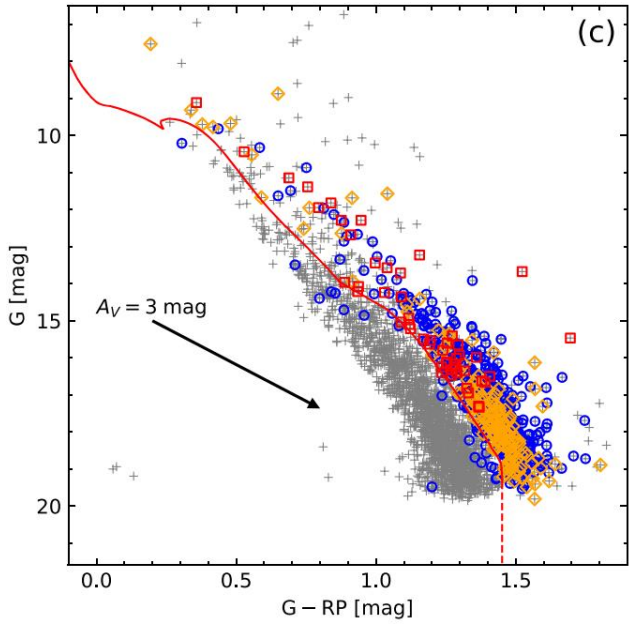

Perseus分子雲のYSOs：LAMOST

55/211がLAMOSTで光学スペクトルを持つ。

38/51は以下の特徴を持つ。

- broad Hα emission (降着活動)
- Li I λ6707 Å absorption lines (若い)

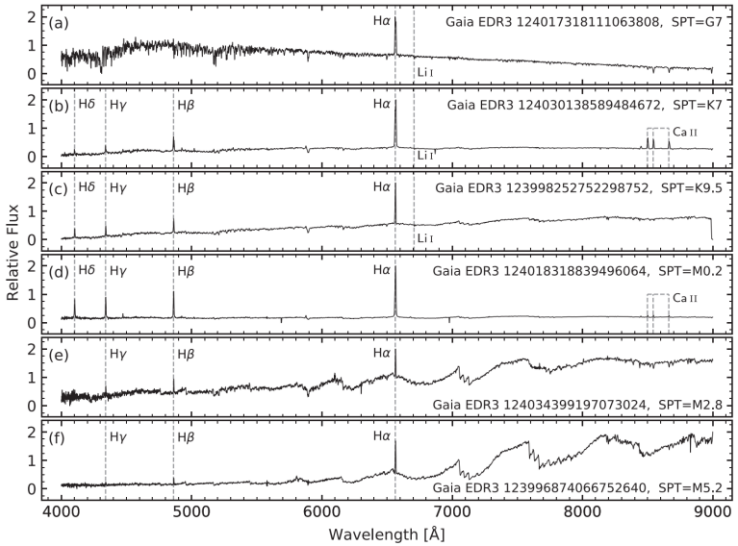

17/51のうち

- 13はHR図上で同じ年代に位置
- 4はMS or AGB stars → 除外

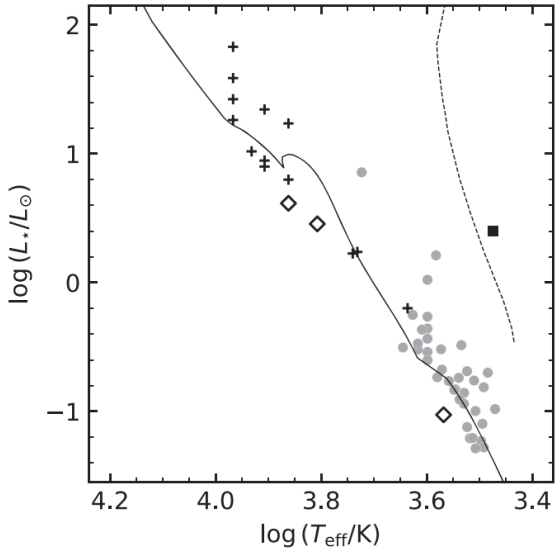

38 + 13 = 51：Perseus分子雲の新たなYSOs

Perseus分子雲のYSOs：51 new members

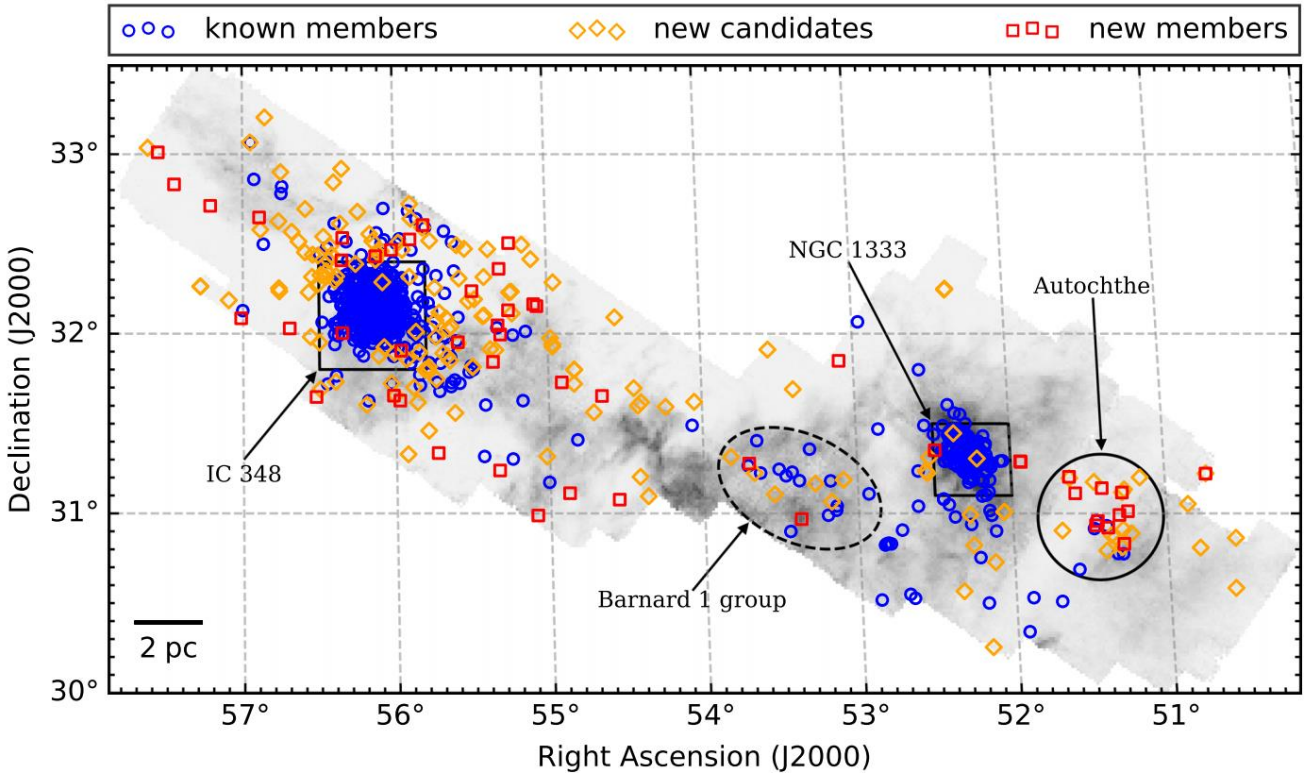

新YSOs (と候補) はガス雲全体に分布する。
(2つの円は今回議論する星集団)

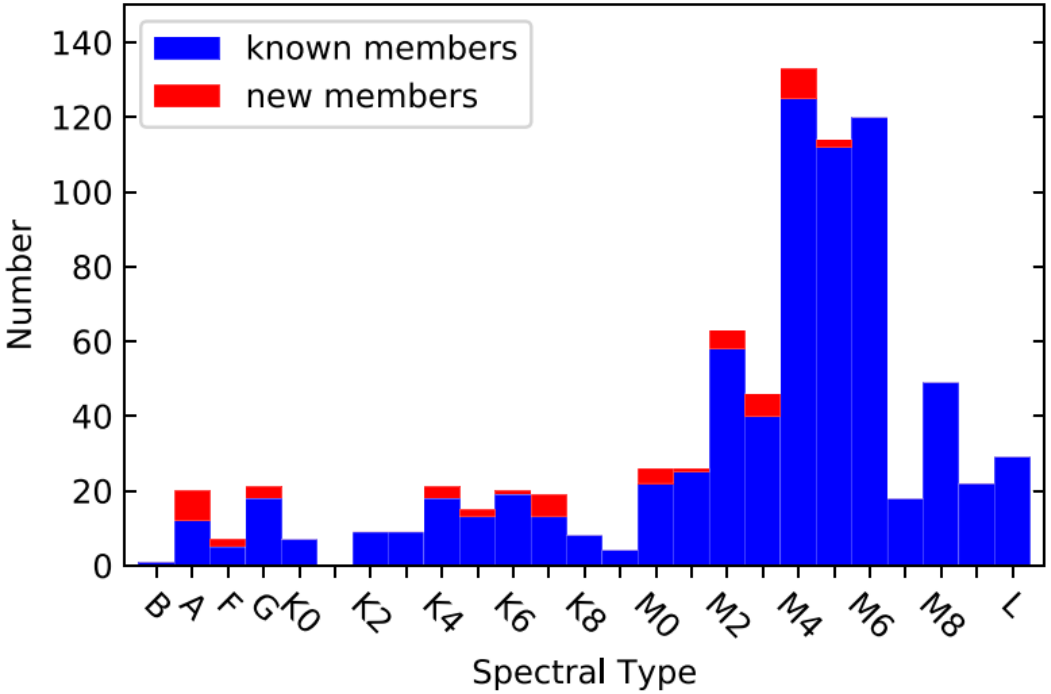

スペクトル型分布への影響はない。
(LAMOST surveyの感度により、M6以降は今回増えない)

Stellar surface densities

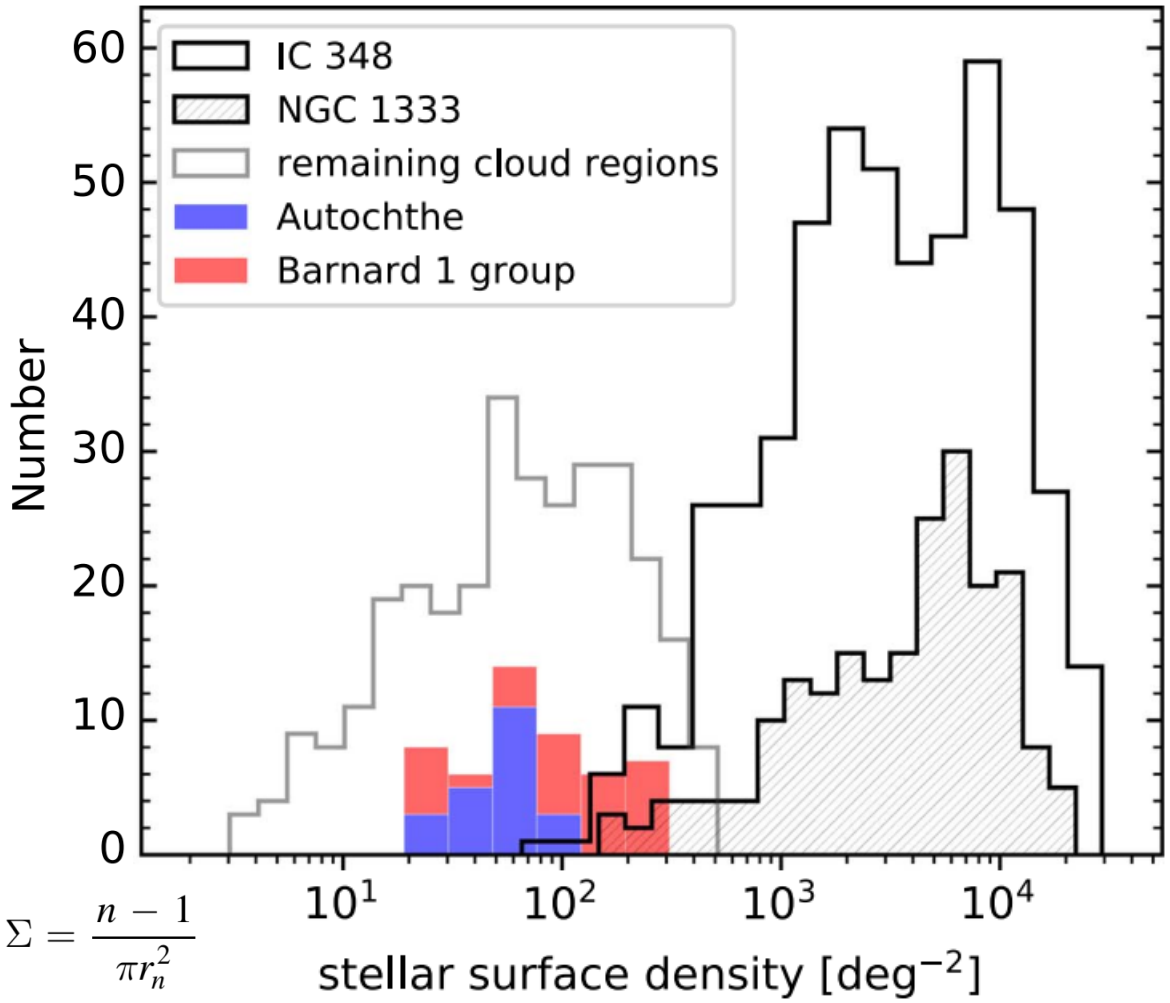

$$\Sigma = \frac{n-1}{\pi r_n^2}$$

We adopt $n = 6$

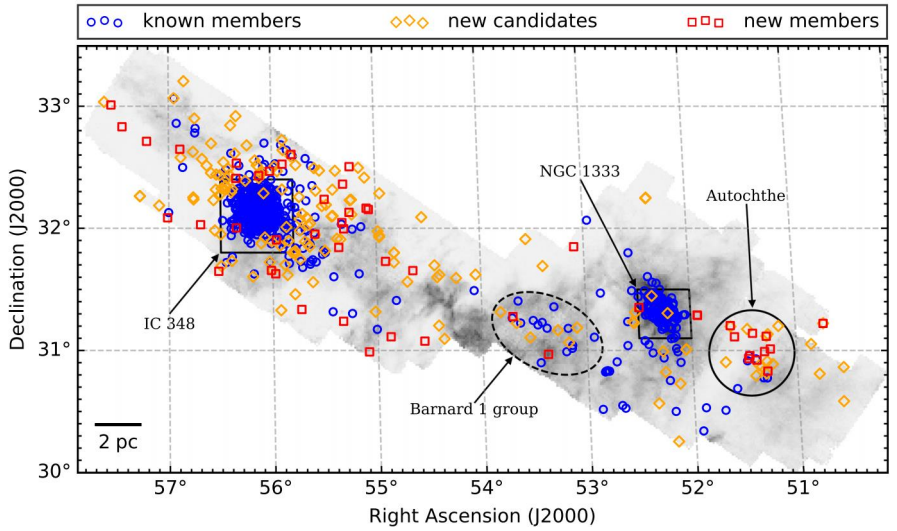

Western aggregate ⇔ dark cloud L1448
(6 known + 10 new + 12 candidates)

East aggregate ⇔ dark cloud Barnard 1
(14 known + 2 new + 6 candidates)

Distance gradient

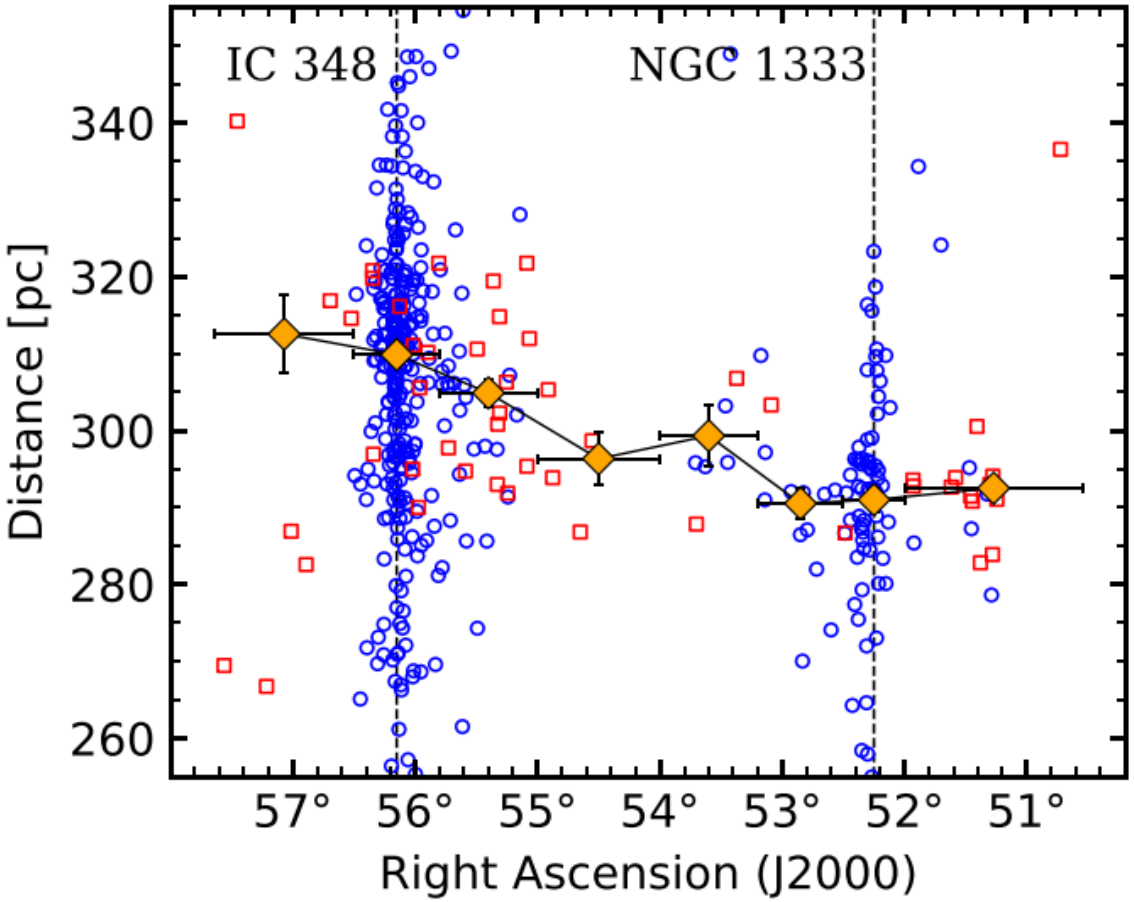

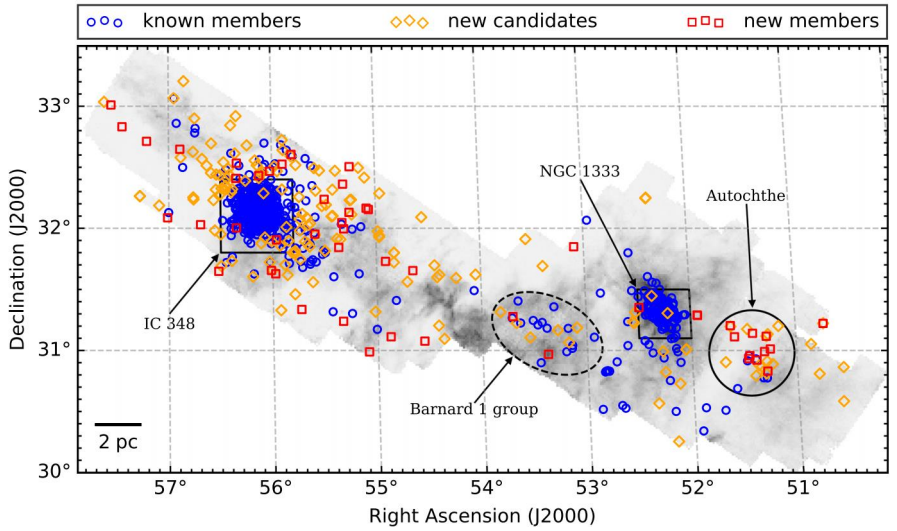

4.84 [pc/deg] from NGC1333 toward IC348

Evolutionary stages

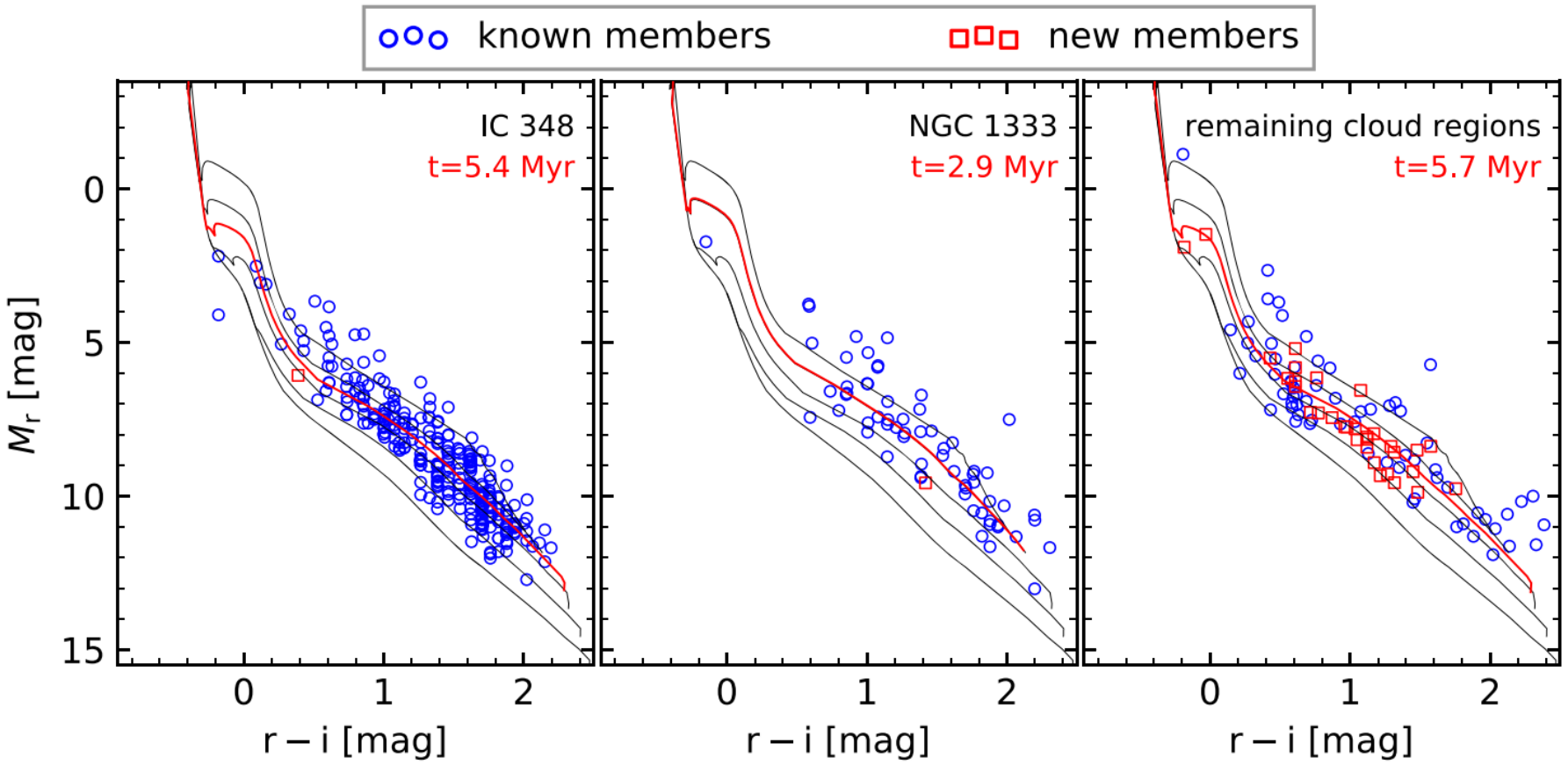

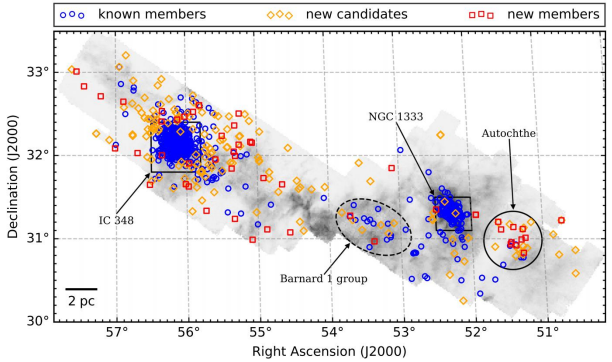

NGC1333よりIC348の方がdiskを持たない天体の割合が大きい ⇔ より古い天体

Perseus分子雲の星形成シナリオ

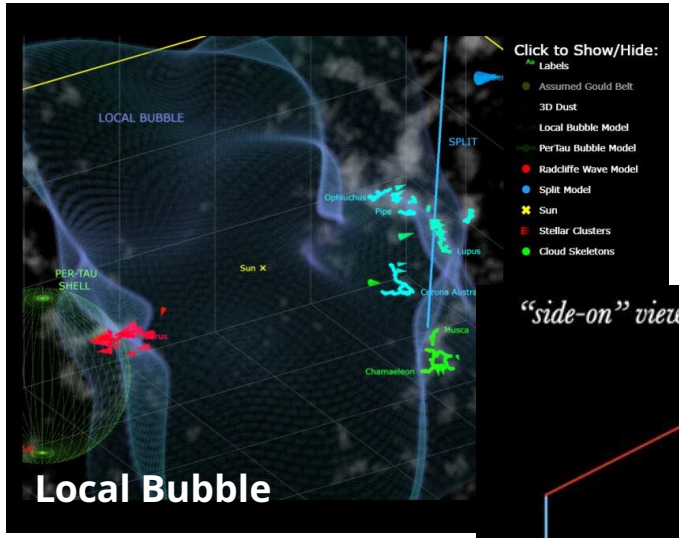

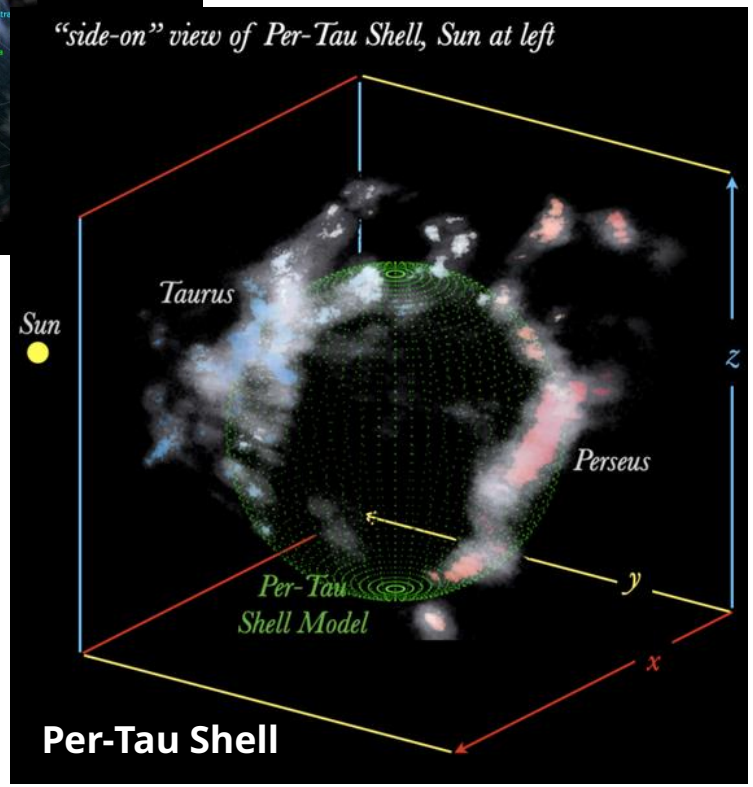

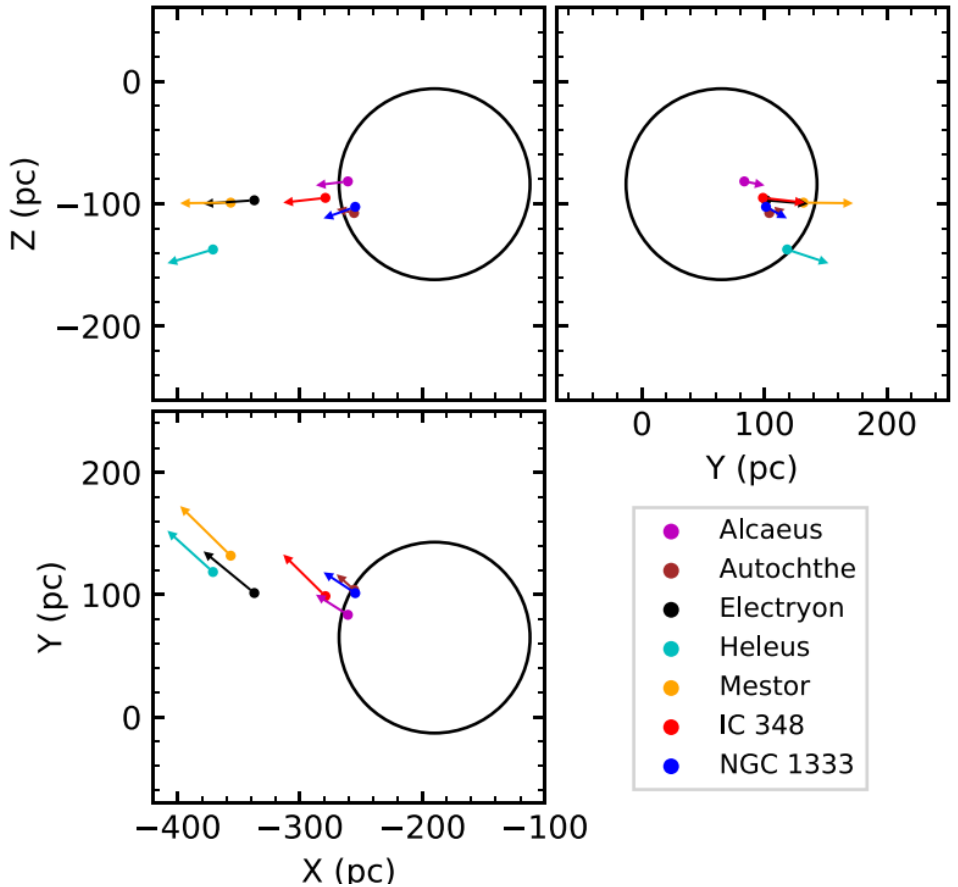

SFN355#29

Probing Magnetic Fields in Protoplanetary Disk Atmospheres through Polarized Near-IR Light Scattered by Aligned Grains

Haifeng Yang (杨海峰)[1,3] and Zhi-Yun Li[2]

Abstract

Magnetic fields play essential roles in protoplanetary disks. Magnetic fields in the disk atmosphere are of particular interest, as they are connected to the wind-launching mechanism. In this work, we study the polarization of the light scattered off of magnetically aligned grains in the disk atmosphere, focusing on the deviation of the polarization orientation from the canonical azimuthal direction, which may be detectable in near-IR polarimetry with instruments such as VLT/SPHERE. We show with a simple disk model that the polarization can even be oriented along the radial (rather than azimuthal) direction, especially in highly inclined disks with toroidally dominated magnetic fields. This polarization reversal is caused by the anisotropy in the polarizability of aligned grains and is thus a telltale sign of such grains. We show that the near-IR light is scattered mostly by μm-sized grains or smaller at the $\tau = 1$ surface and such grains can be magnetically aligned if they contain superparamagnetic inclusions. For comparison with observations, we generate synthetic maps of the ratios of U_ϕ/I and Q_ϕ/I, which can be used to infer the existence of (magnetically) aligned grains through a negative Q_ϕ (polarization reversal) and/or a significant level of U_ϕ/I. We show that two features observed in the existing data, an asymmetric distribution of U_ϕ with respect to the disk minor axis and a spatial distribution of U_ϕ that is predominantly positive or negative, are incompatible with scattering by spherical grains in an axisymmetric disk. They provide indirect evidence for scattering by aligned nonspherical grains.

Characterising the orbit and circumstellar environment of the high-mass binary MWC 166 A

Sebastian A. Zarrilli[1], Stefan Kraus[1], Alexander Kreplin[1], John D. Monnier[2], Tyler Gardner[2], Antoine Mérand[5], Sam Morrell[1], Claire L. Davies[1], Aaron Labdon[1,5], Jacob Ennis[2], Benjamin Setterholm[2], Jean-Baptiste Le Bouquin[3], Narsireddy Anugu[4], Cyprien Lanthermann[4], Gail Schaefer[4], and Theo ten Brummelaar[4]

ABSTRACT

Context. Stellar evolution models are highly dependent on accurate mass estimates, especially for highly massive stars in the early stages of stellar evolution. The most direct method for obtaining model-independent stellar masses is derivation from the orbit of close binaries.

Aims. Our aim was to derive the first astrometric plus radial velocity orbit solution for the single-lined spectroscopic binary star MWC 166 A, based on near-infrared interferometry over multiple epochs and ~100 archival radial velocity measurements, and to derive fundamental stellar parameters from this orbit. A supplementary aim was to model the circumstellar activity in the system from *K* band spectral lines.

Methods. The data used include interferometric observations from the VLTI instruments GRAVITY and PIONIER, as well as the MIRC-X instrument at the CHARA Array. We geometrically modelled the dust continuum to derive relative astrometry at 13 epochs, determine the orbital elements, and constrain individual stellar parameters at five different age estimates. We used the continuum models as a base to examine differential phases, visibilities, and closure phases over the Br γ and He I emission lines in order to characterise the nature of the circumstellar emission.

Results. Our orbit solution suggests a period of $P = 367.7 \pm 0.1$ d, approximately twice as long as found with previous radial velocity orbit fits. We derive a semi-major axis of 2.61 ± 0.04 au at $d = 990 \pm 50$ pc, an eccentricity of 0.498 ± 0.001, and an orbital inclination of $53.6 \pm 0.3°$. This allowed the component masses to be constrained to $M_1 = 12.2 \pm 2.2\,M_\odot$ and $M_2 = 4.9 \pm 0.5\,M_\odot$. The line-emitting gas was found to be localised around the primary and is spatially resolved on scales of ~11 stellar radii, where the spatial displacement between the line wings is consistent with a rotating disc.

Conclusions. The large spatial extent and stable rotation axis orientation measured for the Br γ and He I line emission are inconsistent with an origin in magnetospheric accretion or boundary-layer accretion, but indicate an ionised inner gas disc around this Herbig Be star. We observe line variability that could be explained either with generic line variability in a Herbig star disc or V/R variations in a decretion disc scenario. We have also constrained the age of the system, with relative flux ratios suggesting an age of $\sim(7 \pm 2) \times 10^5$ yr, consistent with the system being composed of a main-sequence primary and a secondary still contracting towards the main-sequence stage.